A Field-Particle Correlation Analysis of a Perpendicular Magnetized Collisionless Shock: I. Theory

Gregory G. Howes†[1], James Juno[2], Jason M. TenBarge[3], Lynn B. Wilson III[4], Damiano Caprioli[5] and Anatoly Spitkovsky[3]

[1]Department of Physics and Astronomy,University of Iowa, Iowa City IA 54224, USA

[2]Institute for Research in Electronics and Applied Physics, University of Maryland, College Park, MD 20742, USA

[3]Department of Astrophysical Sciences, Princeton University, Princeton, NJ 08543, USA

[4] NASA Goddard Space Flight Center, Heliophysics Division, Greenbelt, MD 20771, USA

[5] Department of Astronomy and Astrophysics, University of Chicago, Chicago, Illinois 60637, USA

(Received ?; revised ?; accepted ?. - To be entered by editorial office)

Collisionless shocks play an important role in space and astrophysical plasmas by irreversibly converting the energy of the incoming supersonic plasma flows into other forms, including plasma heat, particle acceleration, and electromagnetic field energy. Here we present the application of the field-particle correlation technique to an idealized perpendicular magnetized collisionless shock to understand the transfer of energy from the incoming flow into ion and electron energy through the structure of the shock. The connection between a Lagrangian perspective following particle trajectories, and an Eulerian perspective observing the net energization of the distribution of particles, illuminates the energy transfer mechanisms. Using the field-particle correlation analysis, we identify the velocity-space signature of shock-drift acceleration of the ions in the shock foot, as well as the velocity-space signature of adiabatic electron heating through the shock ramp.

PACS codes:

1. Introduction

Collisionless shocks play an important role in the heliosphere and other astrophysical plasmas by irreversibly converting the kinetic energy of supersonic plasma flows into other forms, including plasma heat, particle acceleration, and electromagnetic field energy (e.g., Wilson III *et al.* 2010, 2012, 2014*a*,*b*, and references therein). Kinetic numerical simulations and recent spacecraft measurements from the *MMS* mission (Chen *et al.* 2018; Goodrich *et al.* 2018) have enabled researchers to illuminate some aspects of the energy conversion processes in collisionless shocks (*e.g.*, instabilities, cross-shock potential). However, our understanding of the transformation of energy within collisionless shocks remains incomplete. Identifying and characterizing the kinetic plasma physics mechanisms that govern the energization of the particles in collisionless shocks is one of the grand challenge problems in heliophysics.

In general, the shock slows the plasma flow from supersonic to subsonic and collisionless

† Email address for correspondence: gregory-howes@uiowa.edu

interactions within the shock act to transform the kinetic energy lost from the incoming bulk flow into particle kinetic energy and electromagnetic field energy. Energy deposited in the core of the particle velocity distribution generally broadens the distribution about the mean flow velocity and leads to plasma heating; energy transferred to particles in the tail of the distribution generally leads to particle acceleration. Here we use *particle energization* as a generic term that includes both of these possible outcomes, *plasma heating* or *particle acceleration*.

The global dynamics of collisionless shocks are thought to be controlled primarily by two parameters: (i) the fast magnetosonic Mach number M_f and (ii) the shock normal angle θ_{Bn} between the average upstream magnetic field and the normal to the shock surface (Treumann 2009). The qualitative behavior of quasi-perpendicular shocks ($45^\circ \lesssim \theta_{Bn} \leqslant 90^\circ$) is found to differ from that of quasi-parallel shocks ($0^\circ \leqslant \theta_{Bn} \lesssim 45^\circ$) (Treumann 2009; Caprioli & Spitkovsky 2014). If the upstream Mach number exceeds the first critical Mach number $M_{crit,1}$ (Edmiston & Kennel 1984; Kennel *et al.* 1985), the shock will reflect some fraction of the incoming particles in order achieve sufficient dissipation to maintain stationarity. For the usual solar wind conditions, and over a large range of angles θ_{Bn}, the value of this first critical Mach number is typically $M_{crit,1} \lesssim 2$ (Wilson III 2016). The solar wind flow is sufficiently fast that $M_f > M_{crit,1}$, meaning the the Earth's bow shock is most often a *supercritical* collisionless shock (Wilson III 2016).

Although the Rankine-Hugoniot jump conditions provide requirements on the conservation of total mass, momentum, and energy through the shock transition, they do not constrain the partitioning of energy among species (protons, electrons, and minor ions). The ion and electron plasma beta values, β_i and β_e, are two additional key parameters that impact the collisionless transfer of energy between the particles and fields, and may therefore influence the differential energization of the plasma species.

Kinetic instabilities and foreshock phenomena, as well as the potential nonstationary of the shock, may impact the energization of particles at collisionless shocks, but we focus here on the proposed mechanisms for particle acceleration at collisionless shocks. Shock surfing acceleration (SSA) involves reflection of particles by a cross-shock electrostatic potential at the leading edge of the shock ramp and energization by the motional electric field (parallel to the shock front) that supports the plasma inflow through the shock (Sagdeev 1966; Sagdeev & Shapiro 1973; Lever *et al.* 2001; Shapiro & Üçer 2003). Shock drift acceleration (SDA) is similar to SSA, but the particles are reflected instead by the magnetic field gradient in the shock ramp, again gaining energy from the motional electric field (Anagnostopoulos *et al.* 1998; Ball & Melrose 2001; Park *et al.* 2013). Diffusive shock acceleration (DSA) occurs when particles gain energy by reflecting off of converging scattering centers (Fermi 1949, 1954; Blandford & Ostriker 1978; Ellison 1983; Blandford & Eichler 1987; Decker 1988; Malkov & Drury 2001; Caprioli *et al.* 2010). Early work suggested that DSA may be more effective at quasi-perpendicular shocks (Jokipii 1987), but injection presents a problem (Caprioli *et al.* 2015), whereas quasi-parallel ($\theta_{Bn} < 45^\circ$) shocks with self-consistently generated upstream turbulence spontaneously promote thermal particles to energetic ones, and thus can more efficiently accelerate suprathermal particles (Caprioli & Spitkovsky 2014; Park *et al.* 2015). Finally, the "fast Fermi" mechanism energizes particles by a single bounce at the shock ramp, possibly leading to significant electron acceleration for high Mach number shocks or nearly perpendicular shock normal angles $\theta_{Bn} \gtrsim 88^\circ$ (Leroy & Mangeney 1984; Wu 1984; Savoini *et al.* 2010).

All of these key physical processes that govern the evolution of collisionless shocks—including kinetic instabilities, plasma heating, and particle acceleration—fundamentally involve the collisionless transfer of energy between particles and electromagnetic fields.

The primary aim of the present study is to illuminate the details of this energy transfer using the recently developed field-particle correlation technique (Klein & Howes 2016; Howes *et al.* 2017; Klein *et al.* 2017). This innovative method employs the electromagnetic fields and full particle velocity distributions measured at a single spatial point to generate a characteristic *velocity-space signature* of the energy transfer mechanism, providing a new avenue for the identification and quantitative characterization of the underlying plasma physical process responsible for the particle energization.

1.1. *The Field-Particle Correlation Technique*

The Maxwell-Boltzmann equations describe the nonlinear evolution of a kinetic plasma. Under the weakly collisional conditions typical of heliospheric plasmas, we can drop the collision term in the Boltzmann equation, which is negligible on the timescale of the collisionless transfer of energy between fields and particles in collisionless shocks, to obtain the Vlasov equation. The field-particle correlation technique (Klein & Howes 2016; Howes *et al.* 2017; Klein *et al.* 2017) was devised to fully utilize the electromagnetic field and particle velocity distribution function information—provided by both kinetic numerical simulations and spacecraft observations—to diagnose this energy transfer, specifically focusing on particle energization.

To explore the energy transfer between fields and particles, we define the *phase-space energy density* for a particle species s by $w_s(\mathbf{r},\mathbf{v},t) \equiv m_s v^2 f_s(\mathbf{r},\mathbf{v},t)/2$ in the non-relativistic limit. Multiplying the Vlasov equation by $m_s v^2/2$, we obtain an expression for the rate of change of this phase-space energy density,

$$\frac{\partial w_s(\mathbf{r},\mathbf{v},t)}{\partial t} = -\mathbf{v}\cdot\nabla w_s - q_s\frac{v^2}{2}\mathbf{E}\cdot\frac{\partial f_s}{\partial \mathbf{v}} - \frac{q_s}{c}\frac{v^2}{2}\left(\mathbf{v}\times\mathbf{B}\right)\cdot\frac{\partial f_s}{\partial \mathbf{v}}. \tag{1.1}$$

Note that this equation determines the rate of change of w_s at each point in 3D-3V phase space. Integrating over all velocity space and all physical space eliminates the first and third terms (Howes *et al.* 2017; Klein *et al.* 2017) , yielding an equation for the rate of change of the total kinetic energy $\mathcal{W}_s$ of a particle species s

$$\frac{\partial \mathcal{W}_s}{\partial t} = -\int d^3\mathbf{r}\int d^3\mathbf{v}\; q_s\frac{v^2}{2}\frac{\partial f_s}{\partial \mathbf{v}}\cdot\mathbf{E} = \int d^3\mathbf{r}\left(\int d^3\mathbf{v}\; q_s\mathbf{v}f_s\right)\cdot\mathbf{E} = \int d^3\mathbf{r}\;\mathbf{j}_s\cdot\mathbf{E}, \tag{1.2}$$

where an integration by parts in velocity has been used between the second and third forms above. This expression shows that the change in species energy $\mathcal{W}_s$ is due to work done on that species by the electric field, $\mathbf{j}_s\cdot\mathbf{E}$. The two middle expressions also make clear the concept that measurements of the electric field $\mathbf{E}$ and particle velocity distribution $f_s(\mathbf{v})$ provide the information needed to determine the rate of energy transfer between the fields and particle species s.

For application to spacecraft measurements—which are limited to a single point, or at most a few points, in space—we do not have sufficient information to perform the spatial integration in (1.2). But spacecraft can provide measurements of the full 3V particle velocity distribution, so we can use (1.1) to compute the rate of change of phase-space energy density $\partial w_s(\mathbf{r}_0,\mathbf{v})/\partial t$ over the full 3V velocity distribution at a single point in space $\mathbf{r}_0$.

Therefore, we simply evaluate the second term on the right-hand side of (1.1), where we can separate the contributions to the dot product from each of the components of the electric field. For the analysis of perpendicular collisionless shocks presented here†,

† Note that, for the specific case of an exactly perpendicular shock with $\theta_{Bn} = 90^\circ$ examined here, we assume zero electric field component parallel the magnetic field, $E_z = 0$.

where the out-of-plane magnetic field is in the z direction, we define the field-particle correlations at spatial position $\mathbf{r}_0$ by

$$C_{E_x}(\mathbf{v},t,\tau) = C\left(-q_s\frac{v_x^2}{2}\frac{\partial f_s(\mathbf{r}_0,\mathbf{v},t)}{\partial v_x}, E_x(\mathbf{r}_0,t)\right) \tag{1.3}$$

$$C_{E_y}(\mathbf{v},t,\tau) = C\left(-q_s\frac{v_y^2}{2}\frac{\partial f_s(\mathbf{r}_0,\mathbf{v},t)}{\partial v_y}, E_y(\mathbf{r}_0,t)\right). \tag{1.4}$$

Note that the factor v^2 in the second term on the right-hand side of (1.1) has been reduced to v_x^2 in (1.3) and v_y^2 in (1.4), because the components not in the derivative yield zero net energization when integrated over velocity, as discussed in more detail in Appendix A. We also note that, as shown above in (1.2), integration of the correlation C_{E_x} over velocity space simply yields the net rate of work done by that component of the electric field on the plasma species, $j_{sx}E_x$.

For previous applications of the field-particle correlation technique to understand the particle energization in plasma turbulence (Klein & Howes 2016; Klein *et al.* 2017; Howes *et al.* 2017; Howes 2017; Howes *et al.* 2018; Chen *et al.* 2019; Li *et al.* 2019; Klein *et al.* 2020), the correlation in these equations is simply an unnormalized time-average over the chosen correlation interval τ, needed to eliminate the contribution from any conservative oscillating energy transfer associated with undamped wave motion (Klein & Howes 2016; Howes *et al.* 2017). As a first application here, we take the case of stationary collisionless shocks, where the electromagnetic fields associated with the structure of the shock transition region (excluding instability-driven fluctuations) are effectively quasi-static components when viewed in the shock frame. Thus, it is unnecessary to perform the time-average and we simply take $\tau = 0$ for the theoretical analysis of perpendicular shocks presented here. If kinetic instabilities arise upstream or within the shock transition region, or the shock itself becomes nonstationary, then it is likely that taking a correlation interval τ longer than either the unstable wave period or the shock reformation time will be necessary to recover a meaningful velocity-space signature of the net particle energization.

The field-particle correlation technique has achieved several notable successes in application to kinetic simulations of plasma turbulence: the identification of ion Landau damping in removing energy from strong plasma turbulence (Klein *et al.* 2017); showing that the spatially non-uniform particle energization observed in self-consistently generated current sheets occurs through Landau damping (Howes *et al.* 2018); identifying different mechanisms (ion cyclotron damping and ion Landau damping) occurring simultaneously at the same position in a plasma using only single-point measurements (Klein *et al.* 2020); exploring the energy transfer from unstable velocity distributions to electromagnetic fields in kinetic instabilities (Klein 2017); and exploring the particle energization in Fourier space as a function of the wavenumber of turbulent electromagnetic fluctuations (Li *et al.* 2019). But the most significant achievements of the technique to date are the application to *MMS* observations which first definitively identified an interval in which electron Landau damping played a key role in removing energy from the turbulence in the Earth's magnetosheath (Chen *et al.* 2019), and subsequently showed that electron Landau damping was present in 19 of 20 *MMS* intervals studied, with this mechanism dominating the removal of energy from the turbulent cascade in about half of those intervals (Afshari *et al.* 2020). Recent work related to the application of the field-particle correlation technique to *MMS* observations includes the use of multi-point electron velocity distributions at the four spacecraft positions to evaluate the ∇f_e

term in the Vlasov equation and subsequently compute its first moment to determine directly $\nabla \cdot P_e$ within electron scale current sheets in the Earth's magnetopause and magnetosheath (Shuster *et al.* 2019). Here we perform the first application of the field-particle correlation technique to characterize the ion and electron energization in an idealized perpendicular magnetized collisionless shock. A companion paper, (Juno *et al.* 2020) (hereafter Paper II), will apply the same technique to self-consistent kinetic simulations of a perpendicular collisionless shock, validating the velocity-space signatures predicted here.

1.2. *Aims of this Study*

The primary aim is to determine the *velocity-space signatures* of ion and electron energization in collisionless shocks using the field-particle correlation technique. The field-particle correlation technique yields an inherently Eulerian description of the particle energization in the six-dimensional (3D-3V) phase space of a kinetic plasma. Through the single-particle-motion analyses presented here, we strive to make a connection to the more widely employed Lagrangian picture of particle energization using particle-in-cell (PIC) simulation codes, as discussed in Appendix B. For this initial application to shocks, we focus on the most simple case of an exactly perpendicular, magnetized collisionless shock with $\theta_{Bn} = 90°$. We choose a fast magnetosonic Mach number $M_f = 3$, within the supercritical regime $M_f > M_{crit,1}$ that is relevant to the Earth's bowshock (Wilson III 2016).

For a perpendicular shock with a ramp width L, the response of the ions and electrons to the shock transition occupies two distinct regimes, quantified by the limits of the ratio of the particle thermal Larmor radius $\rho_s \equiv v_{ts}/\Omega_s$ to the shock ramp width: (i) in the ion regime, $\rho_i/L \gtrsim 1$, and (ii) in the electron regime, $\rho_e/L \ll 1$. In these regimes, the evolution of the ion velocity distribution certainly violates adiabatic invariance, whereas the response of the electrons to the shock ramp structure is expected to be dominated by the adiabatic response (neglecting the possible effect of kinetic instabilities that may generate fluctuations in the shock transition with length scales on the order of ρ_e). Of course, for higher energy particles in the suprathermal tails, violation of the adiabatic invariance is much more likely, even for electrons. To understand the energization of ions and electrons at an idealized shock ramp, we treat these two limits separately in the next two sections.

2. Ion Energization at an Idealized Perpendicular Magnetized Collisionless Shock

To analyze the energization of ions at a perpendicular collisionless shock, we specify an idealized model of a perpendicular shock consisting of a perpendicular magnetic field $\mathbf{B} = B(x)\hat{\mathbf{z}}$ with a magnetic discontinuity at $x = 0$ given by

$$B(x) = \begin{cases} B_u & x \geqslant 0 \\ B_d & x < 0 \end{cases} \tag{2.1}$$

with amplitude jump $B_d/B_u = 4$. In the shock frame of reference, a constant and uniform motional electric field $E_y < 0$ leads to an inflow at the $\mathbf{E} \times \mathbf{B}$ velocity given by $\mathbf{U}(x) = E_y/B(x)\hat{\mathbf{x}} < 0$ with an upstream Alfvén Mach Number $M_A = U_{E\times B}/v_A = 4.9$ and a flow velocity ratio $U_d/U_u = 1/4$. This simple model has no variation in the cross-shock potential, and therefore no electric field component in the shock normal direction, $E_x = 0$. The width of the velocity distribution in the upstream frame (effectively the upstream ion temperature) is characterized by an ion plasma beta $\beta_i = 8\pi n_i T_i/B_0^2 = 1.3$,

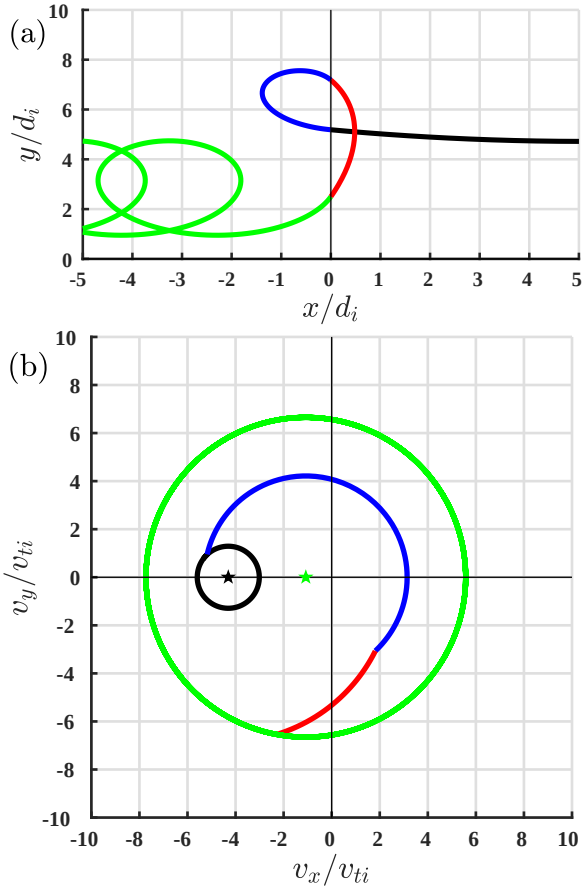

FIGURE 1. (a) Real space trajectory of an ion as it traverses the shock front and (b) velocity space trajectory .

and we specify the electron plasma beta to be $\beta_e = 0.7$. Under these conditions, we obtain an Alfvénic Mach number $M_A = 4.9$, a sonic Mach number $M_s = 3.8$, and a fast magnetosonic Mach number $M_f = 3.0$, putting this perpendicular shock in the super-critical regime. Table 1 in Appendix C provides definitions of relevant characteristic velocities, plasma beta values, and Mach numbers. Although this simple shock model has no cross-shock potential and the compression ratio is not determined self-consistently relative to the upstream Mach number, the model nonetheless provides valuable intuition about the ion energization process and its signature in velocity space, which is the primary aim of this study.

This idealized model of a shock as a magnetic discontinuity corresponds to the limit $\rho_i/L \to \infty$, where L is the characteristic width of the shock transition, so this limit lies on the correct side of the boundary between the regimes where we expect dominantly adiabatic evolution when $\rho_s/L \ll 1$ and where we expect non-adiabatic evolution when $\rho_s/L \gtrsim 1$. As will be shown in Paper II (Juno *et al.* 2020), the qualitative behavior of the ions remains similar between this simple model of a shock as a magnetic discontinuity with $\rho_i/L \gg 1$ and a realistic shock ramp with a width on the order of the ion Larmor radius $\rho_i/L \gtrsim 1$.

A single-particle-motion analysis of the ion trajectory through both configuration space and velocity space provides valuable intuition for interpreting the results of a field-particle

correlation analysis of the ion energization in this idealized perpendicular shock model. In Fig. 1, we plot (a) the trajectory of an ion in the (x, y) plane and (b) its corresponding trajectory in (v_x, v_y) velocity space in the shock frame, where the colors indicate the corresponding segments of the trajectory. In the upstream region at $x > 0$ (black), the black circle centered about the upstream $\mathbf{E} \times \mathbf{B}$ velocity (black star) corresponds to the Larmor orbit of the ion about the upstream inflow velocity in the (v_x, v_y) plane. Upon first crossing the magnetic discontinuity to $x < 0$, the ion changes to a Larmor gyration in the (v_x, v_y) plane (blue) about the downstream $\mathbf{E} \times \mathbf{B}$ velocity (green star). In the larger amplitude downstream perpendicular magnetic field, the radius of the Larmor motion in the (x, y) plane in the shock frame is reduced (blue), and under appropriate conditions (see below), it can lead to the ion crossing back upstream to $x > 0$ (red).

When the ion passes back upstream to $x > 0$, it will once again undergo a Larmor orbit in the (v_x, v_y) plane (red) about the upstream $\mathbf{E} \times \mathbf{B}$ velocity (black star). In this segment of the trajectory (red), the ion gains perpendicular energy in the shock frame, graphically represented by the distance in velocity space of the ion from the origin of the (v_x, v_y) plane. This process of ion energization will be discussed further below. Finally, the ion will eventually cross back into the downstream region to $x < 0$ (green), resuming its Larmor orbit in the (v_x, v_y) plane (green) about the downstream $\mathbf{E} \times \mathbf{B}$ velocity (green star). Without any additional crossings of the magnetic discontinuity, the ion will simply $\mathbf{E} \times \mathbf{B}$ drift downstream.

What mechanism leads to ion energization at the magnetic discontinuity in our idealized perpendicular shock model? In this simple single-particle-motion model, the ion energy can only change due to work done on the ion by the motional electric field, $E_y < 0$. Sufficiently far away upstream or downstream from the magnetic discontinuity that the ion Larmor orbit does not cross $x = 0$, the ion gains and loses energy in the shock frame as it undergoes its Larmor orbit (black and green circles) about the $\mathbf{E} \times \mathbf{B}$ drift velocity (black and green stars), but the ion will experience no net energization over a complete Larmor orbit. Therefore, the ion only experiences a meaningful change in energy in the vicinity of the shock, as expected.

As shown in Fig. 1(b), after first crossing the magnetic discontinuity at $x = 0$, the ion actually loses energy in the shock frame (blue) before crossing back upstream. This is a consequence of the fact that the trajectory downstream (blue) circles about the downstream flow velocity (green star), which brings the ion closer to the origin. However, during its brief foray back upstream (red), the ion will once again encircle the downstream flow velocity (black star), causing the ion to rapidly gain energy, moving further away from the origin. Physically, this is a result of the motional electric field $E_y < 0$ doing positive work on the ion, which is moving in the $-y$ direction, as seen in Fig. 1(a). This well-known energization mechanism is called Shock Drift Acceleration (SDA) (Anagnostopoulos *et al.* 1998; Ball & Melrose 2001; Lever *et al.* 2001; Park *et al.* 2013).

2.1. *Velocity-Space Signature of Shock Drift Acceleration*

Although the single-particle-motion analysis above is valuable for building intuition about the ion energization process, we must examine how the entire ion velocity distribution evolves through the shock transition to provide the context needed to interpret the results of a field-particle correlation analysis of a perpendicular collisionless shock. We use a Vlasov mapping technique, described in Appendix D, to determine the velocity distribution at several key points through the shock transition, denoted by vertical red lines in Fig. 2, where we present (a) the perpendicular magnetic field B_z (blue) and the motional electric field E_y (red) in the shock frame for our idealized shock model, (b) the same

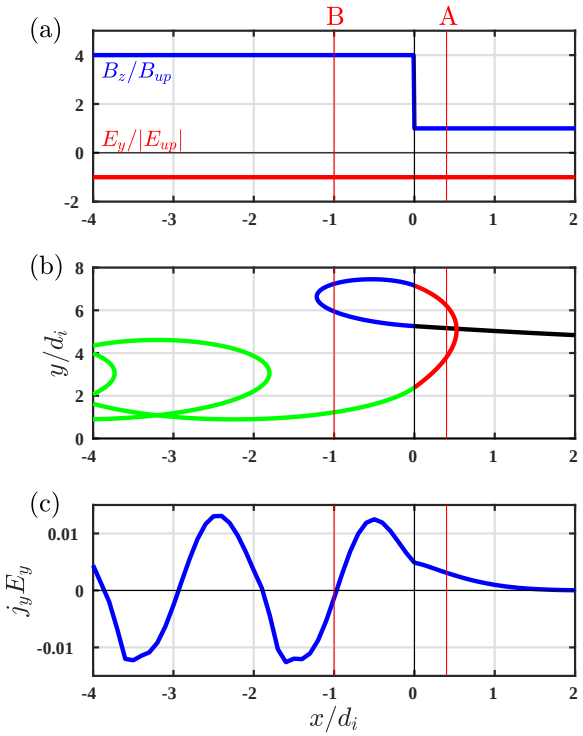

FIGURE 2. (a) Profiles along the shock normal direction of the transverse magnetic field B_z (blue) and the motional electric field E_y (red), (b) trajectory of a reflected ion in the (x, y) plane, and (c) the rate of work done by the electric field on the distribution of particles j_yE_y.

typical trajectory of the ion in the (x, y) plane as shown in Fig. 1(a), and (c) the rate of work done by the motional electric field E_y on the ions, j_yE_y, as a function of distance along the shock normal x. Upstream at $x/d_i \geqslant 2$, the ions are flowing toward the shock at the upstream $\mathbf{E} \times \mathbf{B}$ velocity, so there is zero net energization of the ions, as shown in (c).

At position $x_A = 0.4d_i$, we show in Fig. 3(a) the ion distribution $f_i(v_x, v_y)$ where, in addition to the incoming upstream population centered at the upstream $\mathbf{E} \times \mathbf{B}$ velocity, a component of reflected particles that have returned upstream is seen at $v_y < 0$ and $-4 \lesssim v_x/v_{ti} \lesssim 2$. Overplotted on the distribution is the trajectory in (v_x, v_y) for the ion analyzed in Fig. 1, showing that this reflected population indeed corresponds to the red segment of the trajectory in that figure. We compute the field-particle correlation $C_{E_y}(v_x, v_y)$ that determines the energization of ions by the motional electric field, as shown in Fig. 3(b). Here we see that the energization of ions at this position is completely dominated by this small population of reflected particles. Integrating this field-particle correlation over velocity space simply yields the net rate of work done by E_y, $\int C_{E_y}(v_x, v_y)dv_xdv_y = j_yE_y$, and Fig. 2(c) shows that the work done on the ions here is positive. Therefore, the reflected ions are being energized here. Fig. 3(b) shows the *velocity-space signature of shock-drift acceleration*, the first key result of this paper. Although this reflected population of ions at perpendicular shocks is well established observationally (Paschmann *et al.* 1982; Sckopke *et al.* 1983; Thomsen *et al.* 1985; Gosling *et al.* 1989; Sckopke *et al.* 1990) and theoretically (Gedalin 1996*a*,*b*, 1997; Gedalin *et al.* 2000, 2018), the field-particle correlation analysis makes clear that the ion

energization is dominated here by the reflected population, where the incoming ion beam experiences negligible energization.

At position $x_A = -1.0d_i$, we plot in Fig. 3(c) the ion distribution $f_i(v_x, v_y)$, showing three distinct populations. The single-particle-motion trajectory shown in Fig. 2(b) provides a context for interpreting this complicated velocity distribution. The three populations correspond directly to the three trajectories that pass through $x_A = -1.0d_i$: (i) the population at $v_x < 0$ and $v_y > 0$ corresponds to the first pass through x_A (lower blue segment); (ii) the population at $v_x > 0$ and $v_y \sim 0$ corresponds to the ions that have turned back toward the magnetic discontinuity due to the increased downstream magnetic field, (upper blue segment); and (iii) the population at $v_x < 0$ and $v_y < 0$ corresponds to the ions that have been reflected back upstream and then passed through the discontinuity again to be swept downstream (green). The field-particle correlation $C_{E_y}(v_x, v_y)$, shown in Fig. 3(d), has a somewhat complicated structure, but the rate of energy transfer as a function of (v_x, v_y) is generally odd about $v_y = 0$, meaning there is little net rate of energization, as confirmed by $j_y E_y \simeq 0$ at x_A in Fig. 2(c).

Note that, when the plasma has passed downstream well beyond the magnetic discontinuity, the ions simply undergo a downstream $\mathbf{E} \times \mathbf{B}$ drift, with zero net energization. Examination of Fig. 2(c) at $x < 0$ indeed confirms this expectation, where the rate of work done, given by $j_y E_y$, simply oscillates about zero. In fact, the only part of $j_y E_y$ that is not balanced between positive and negative oscillations is in the foot of the shock at $0 \leqslant x/d_i \lesssim 1$, where the shock drift acceleration occurs. Therefore, this is where all of the net energization of ions *in the shock frame* occurs. Furthermore, by examining the field-particle correlation in Fig. 3(b), we see that the entire net energy gain here occurs in the small fraction of particles in the suprathermal tail of the distribution that are reflected at the shock front.

One may ask, don't the large fraction of protons in the core of the distribution, which broadens in the plane perpendicular to the magnetic field when going through the shock, together have a much larger total gain of energy than the small fraction of particles undergoing shock drift acceleration? Of course, breadth of the distribution in velocity perpendicular to the magnetic field in the downstream frame of reference (velocity space centered at the downstream $\mathbf{E} \times \mathbf{B}$ velocity, given by the green star in Fig. 1) increases significantly relative to much more narrow perpendicular velocity distribution upstream. This can be clearly illustrated by computing a spatially averaged downstream velocity distribution†, as shown in Fig. 3(e) $\langle f_i(v_x, v_y) \rangle$, where we spatially average over $-4 \leqslant x/d_i \leqslant -2$, showing a ring distribution that yields a much larger effective perpendicular temperature when taking the appropriate second moment of the distribution in the downstream frame of reference. But, when viewed in the downstream frame of reference centered at the green star in Fig. 1, the protons in the core of the distribution that end up forming the (spatially averaged) ring distribution experience no net gain in energy upon passing through the shock. Instead, the energy of these protons changes form from the directed kinetic energy of the upstream flow into a broad ring distribution with a much larger effective perpendicular temperature. This conversion conserves energy, of course, so the total microscopic kinetic energy of the velocity distribution does not change in this process, and therefore, by (1.2), electric field does no net work on these protons. Downstream of the shock, the field-particle correlation $C_{E_y}(v_x, v_y)$, shown in Fig. 3(f), is again odd about $v_y = 0$, thereby yielding a negligible net rate of energization.

A caveat in this analysis, of course, is that the electromagnetic fields are not derived

† Spatially averaged distributions are likely necessary to make direct comparisons to spacecraft observations due to the finite time required to build up a full velocity distribution.

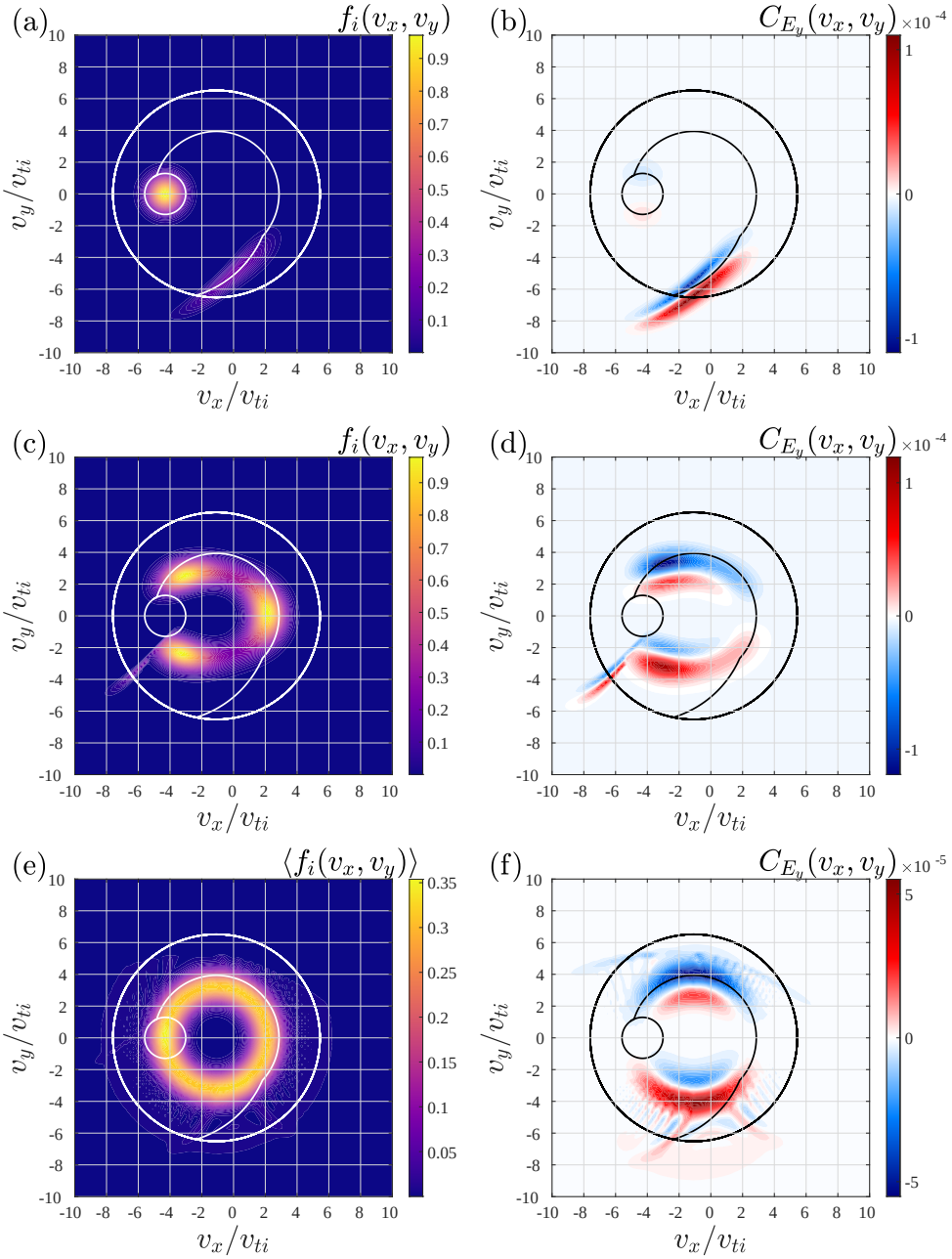

FIGURE 3. Plots of the ion velocity distribution $f_i(v_x, v_y)$ and field-particle correlation C_{E_y} within the shock foot at $x_A/d_i = 0.4$ (a,b) and just downstream of the discontinuity at $x_B/d_i = -1$ (c,d). Averaging over the downstream range $-4 \leqslant x/d_i \leqslant -2$ yields (e) the distribution function $\langle f_i(v_x, v_y) \rangle$ and the field-particle correlation C_{E_y} of the averaged distribution.
.

self-consistently from the velocity distributions, but this analysis nonetheless provides valuable intuition into the nature of particle acceleration at collisionless shocks. Furthermore, the Vlasov mapping analysis eliminates any thermalization of the ion velocity distribution downstream due to collisions or scattering by the kinetic-instability-driven fluctuations that are typically seen in observations or found in simulations of supercritical collisionless shocks. It will be necessary to determine whether the features shown in Fig. 3—in particular, the velocity-space signature of shock drift acceleration shown in panel (b)—persists in self-consistent simulations of collisionless shocks, which is the topic of Paper II.

With the exception of the novel field-particle analysis of the perpendicular shock and the resulting velocity-space signature of shock drift acceleration in Fig. 3(b), the findings about ion energization presented in this section confirm previous findings in the literature, particularly the early work of Gedalin (Gedalin 1996*a*,*b*, 1997; Gedalin *et al.* 2000). In fact, the analysis of Gedalin included more physical effects than are analyzed here, in particular a cross-shock potential. The motivation of the more simplified picture here, however, was to establish the minimum number of elements needed to explain the velocity-space signature of shock drift acceleration found in a simulation of a perpendicular collisionless shock presented in Paper II. Tests indicate that the existence of a cross-shock potential is not necessary to obtain the qualitative appearance of that velocity-space signature, although its presence will, of course, alter the quantitative evolution of the ion energization, as will be detailed in Paper II.

3. Electron Energization at an Idealized Perpendicular Magnetized Collisionless Shock

To explore the electron energization, we take essentially the same shock model as for the ions, but instead of a magnetic discontinuity we take a linear ramp over length $L = 2d_i$, raising the magnetic field magnitude by a factor of $B_d/B_u = 4$. Specifying a realistic proton-to-electron mass ratio $m_i/m_e = 1836$, we satisfy the condition that the electron Larmor radius is much smaller than the width of the shock ramp, $\rho_e/L \ll 1$. Other parameters are the same: a constant and uniform motional electric field $E_y < 0$ in the shock frame, giving an upstream Alfvén Mach Number $M_A = u_{E\times B}/v_A = 4.9$; zero cross shock potential yielding $E_x = 0$; a flow velocity ratio $U_d/U_u = 1/4$; the ion plasma beta $\beta_i = 1.3$ and electron plasma beta $\beta_e = 0.7$; and a sonic Mach number $M_s = 3.8$ and fast magnetosonic Mach number $M_f = 3.0$.

In this model, the increase in the magnetic field magnitude through the ramp leads to a steady decrease in the $\mathbf{E}\times\mathbf{B}$ velocity as the plasma flows through the shock transition. In addition, the gradient in the normal direction of the magnetic field magnitude through the ramp induces a ∇B drift in the $+y$ direction. As we shall see, it is the ∇B drift that leads to the energization of the electrons by the motional electric field, E_y.

Again we begin with a single-particle-motion analysis of the electron motion through this idealized shock model to provide intuition for interpreting the field-particle correlation analysis of the electron energization. In Fig. 4, we plot (a) the profile of the perpendicular magnetic field $B_z(x)$ (blue) and the motional electric field $E_y(x)$ (red) along the shock normal direction, as well as (b) the trajectory of an electron in the (x, y) plane as it flows through the shock ramp over $0 \leqslant x/d_i \leqslant 2$. The trajectory plot shows clearly the ∇B drift in the $+y$ direction. A salient difference between the single particle motion for electrons and ions is that the electron thermal velocity is larger than the inflow velocity, so electrons can move in the $+x$ direction even upstream of the shock.

In the absence of any additional drifts, the electric field E_y supporting the $\mathbf{E}\times\mathbf{B}$ drift

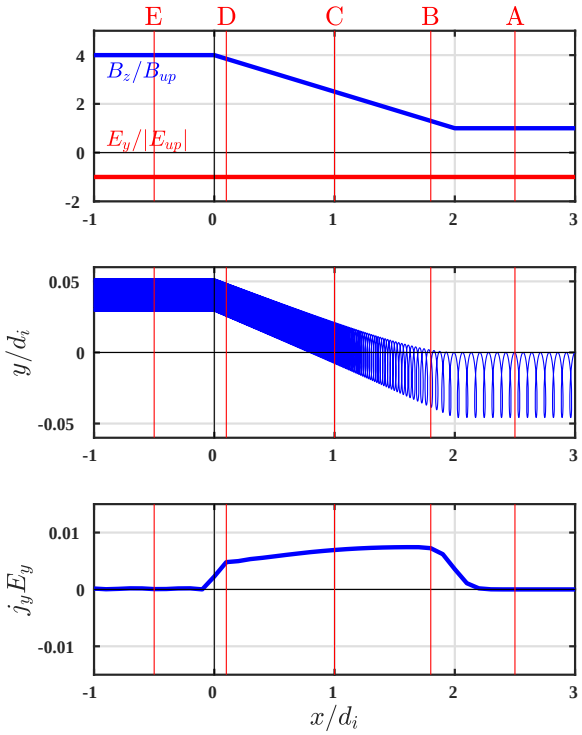

FIGURE 4. (a) Profiles along the shock normal direction of the perpendicular magnetic field B_z (blue) and the motional electric field E_y (red), (b) trajectory of a reflected ion in the (x, y) plane, and (c) the rate of work done by the electric field on the distribution of particles j_yE_y. .

yields zero net electron energization. However, in the region where the perpendicular magnetic field changes magnitude, $0 \leqslant x/d_i \leqslant 2$, there arises a ∇B drift in the $+y$ direction, which indeed leads to a net energization of the electrons by E_y. The rate of energization of the electrons by the ∇B drift in the motional electric field is precisely that needed to conserve the magnetic moment of the electron $\mu = m_e v_\perp^2/2B_z$, leading to adiabatic heating. This can be shown in general by calculating the net rate of work done by E_y due to the ∇B drift, which can change the perpendicular kinetic energy of the electrons,

$$\frac{dm_e v_\perp^2/2}{dt} = q_e u_{\nabla B} E_y \tag{3.1}$$

where the magnitude of the ∇B drift in the $+y$ direction is given by

$$u_{\nabla B} = \frac{m_e v_\perp^2}{2q_e B_z}\left(\frac{1}{B_z}\frac{\partial B_z}{\partial x}\right). \tag{3.2}$$

For the static fields in this model, the total time derivative is dominated by the $\mathbf{E}\times\mathbf{B}$ velocity, $d/dt = \partial/\partial t + u_x\partial/\partial x = u_{E\times B}\partial/\partial x$. Substituting $u_{E\times B} = E_y/B_z$, we can manipulate (3.1) to obtain

$$\frac{\partial}{\partial x}\frac{m_e v_\perp^2}{2B_z} = \frac{\partial \mu}{\partial x} = 0, \tag{3.3}$$

proving that the electron's magnetic moment μ is conserved.

Therefore, we see that, in the limit $\rho_e/L \ll 1$, the electron energization in this simple model is adiabatic, where the energy gain arises due to the ∇B drift perpendicular to

the shock normal. Violation of the adiabatic invariance for electrons in real shocks, of course, may occur due to fluctuations on scales $l \sim d_e$ caused by kinetic instabilities arising either upstream or in the shock transition layer.

3.1. *Velocity-Space Signature of Adiabatic Electron Heating*

The Vlasov mapping technique is used to determine the evolution of the electron distribution function through this perpendicular shock modeled as a linear ramp in the magnetic field magnitude. In Fig. 5, we plot the electron velocity distribution $f_e(v_x, v_y)$ and field-particle correlation C_{E_y} at the positions A, B, C, and D, shown by the vertical red lines in Fig. 4. The net rate of electron energization $j_y E_y = \int dv_x dv_y C_{E_y}(v_x, v_y)$ is also plotted in Fig. 4(c), showing that the net electron energization occurs only within the shock ramp, where the ∇B drift leads to energization by the motional electric field E_y. Upstream of the shock ramp at $x_A/d_i = 2.5$, the field-particle correlation C_{E_y} in Fig. 5(b) shows a velocity-space signature that is exactly odd in v_y, yielding zero net energization of the electrons in this region, as expected for a plasma that is simply undergoing a steady $\mathbf{E} \times \mathbf{B}$ drift. In fact, the magnetic field terms in (1.2), which are not evaluated in the correlation C_{E_y}, exactly cancel the change in the phase space energy density by the electric field E_y, leading to zero net change in the phase space energy density throughout velocity space, as proven in Appendix E.

After entering the finite-width shock ramp, the field-particle correlation C_{E_y} becomes slightly asymmetric, shifted slightly in the $+v_y$ direction due to the ∇B drift, shown in Fig. 5(d), (f), and (h). Although a large part of this energy transfer rate represented by this velocity-space signature cancels out upon integration over v_y, the slight asymmetry leads to a net positive energization of the electrons. As shown by (3.3), this energization of the electrons preserves their magnetic moment μ, and therefore the electron velocity distribution will be adiabatically heated, conserving $T_{e\perp}/B_z$†. Thus, the field-particle correlations C_{E_y} in Fig. 5(d), (f), and (h) show the *velocity-space signature of adiabatic electron heating*, with the slight asymmetry in the pattern leading to the net positive energization of the electrons needed to conserve $T_{e\perp}/B_z$ in the increasing perpendicular magnetic field amplitude through the shock ramp. This velocity-space signature is the second key result of this paper.

Note that the magnitude of the drifts relative to the electron thermal velocity are very small for this case, with values $u_{E\times B}/v_{te} = 0.14$ and $u_{\nabla B}(v_\perp = v_{te})/v_{te} = 0.037$. Therefore, the shifts of the center of the electron velocity distributions $f_e(v_x, v_y)$ away from the origin in the plots shown in Fig. 5 are very small, and the corresponding asymmetries in the velocity-space signatures are likewise small. Because of the difficulty in visualizing these slight asymmetries in the field-particle correlation C_{E_y}, we present in Fig. 6 cuts along v_y through the center of the velocity distribution (at the local $\mathbf{E} \times \mathbf{B}$ velocity, $U_x = u_{E\times B}$) for each of the x positions A–E noted in Fig. 4. Upstream of the ramp at x_A (blue), the correlation $C_{E_y}(v_y)$ is exactly odd in v_y, leading to zero net electron energization. Inside the shock ramp at x_B (red), the asymmetry between the rate of energy loss at $v_y < 0$ and rate of energy gain at $v_y > 0$ becomes apparent, yielding a net electron energization. The same asymmetries are observed at x_C (green) and x_D (black). Downstream of the shock ramp, at x_E (magenta), $C_{E_y}(v_y)$ becomes odd about $v_y = 0$ once again, indicating a cessation of the electron energization, as shown in Fig. 4(c).

† Note that the perpendicular temperature is computed relative to the local electron drift velocity, which includes both the $\mathbf{E} \times \mathbf{B}$ and ∇B drifts.

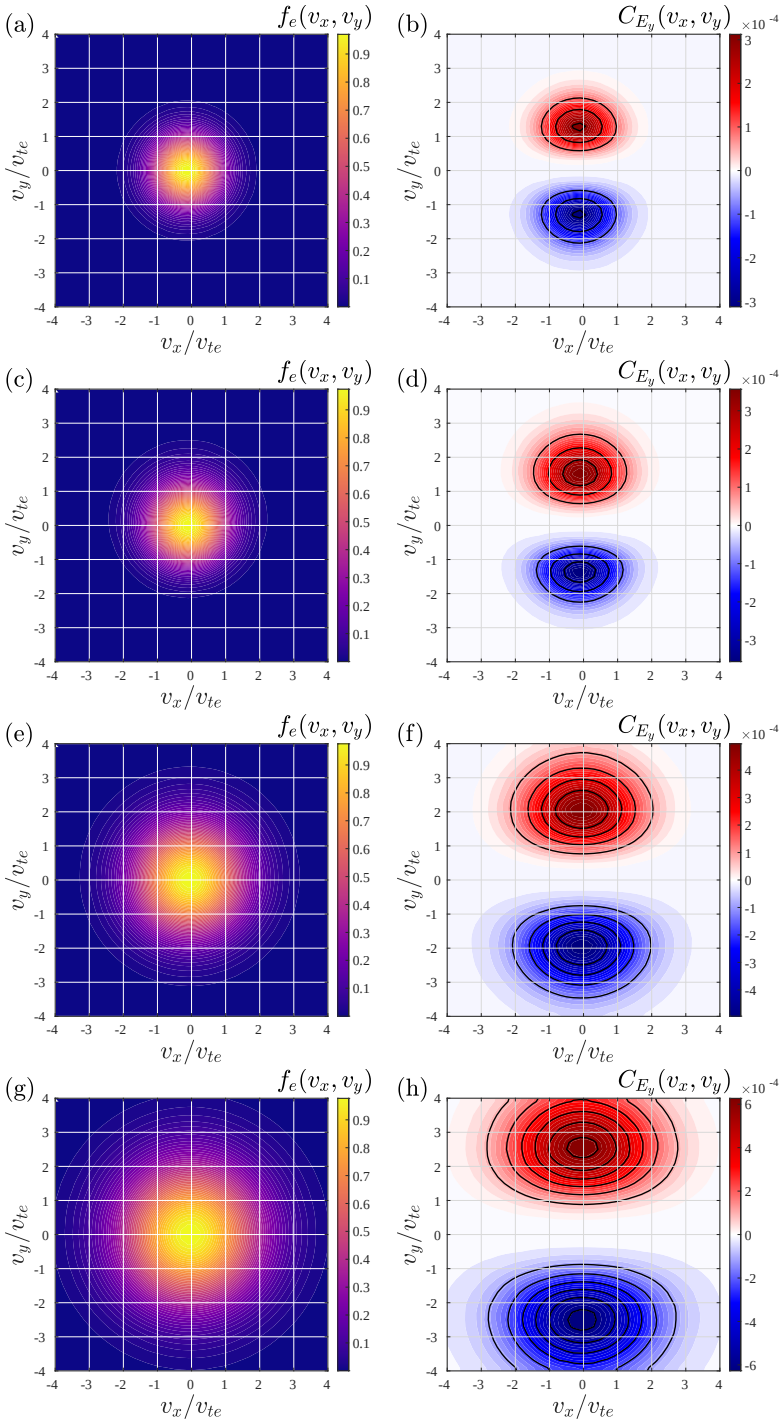

FIGURE 5. Plots of the electron velocity distribution $f_e(v_x, v_y)$ and field-particle correlation C_{E_y} within the shock foot at $x_A/d_i = 2.5$ (a,b), at $x_B/d_i = 1.8$ (c,d), at $x_C/d_i = 1.0$ (e,f), and at $x_D/d_i = 0.1$ (g,h). .

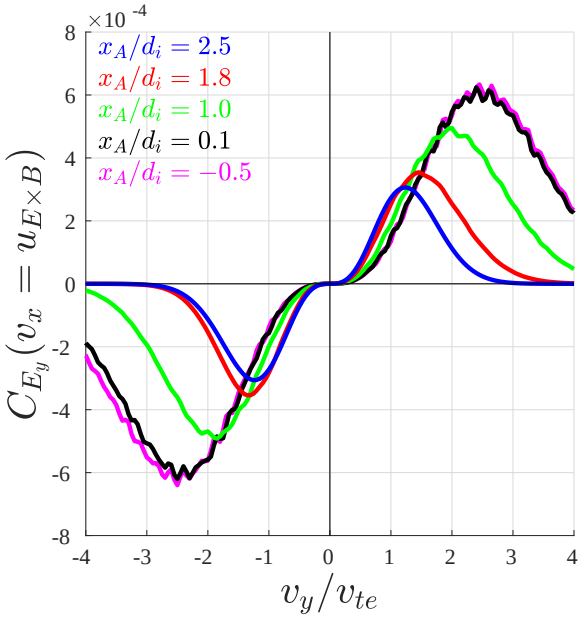

FIGURE 6. (a) Cuts along v_y through the center of the velocity distribution (at the local $\mathbf{E}\times\mathbf{B}$ velocity, $U_x = u_{E\times B}$), of the field-particle correlation C_{E_y}. .

4. Theory for Ion Energization at a Magnetic Discontinuity

Although based on an idealized model, useful intuition into the energization of ions at perpendicular collisionless shocks can be gained by a simple analysis of the energy gain due to the flow through a magnetic discontinuity with a jump in the perpendicular magnetic field magnitude, $1 < B_d/B_u \leqslant 4$. The single particle motion analysis in Fig. 1 shows that, upstream of the magnetic discontinuity at $x > 0$, the ions undergo gyration in velocity space (black circle) about the upstream $\mathbf{E}\times\mathbf{B}$ velocity (black star). Downstream of the magnetic discontinuity at $x < 0$, the ions undergo gyration in velocity space (green circle) about the downstream $\mathbf{E}\times\mathbf{B}$ velocity (green star). In general, as ions pass through the magnetic discontinuity, the perpendicular velocity (in the local bulk-flow frame of reference) increases at the expense of the diminished bulk-flow velocity (given by the local $\mathbf{E}\times\mathbf{B}$ velocity).

For this simple model, the downstream perpendicular velocity relative to the upstream bulk-flow velocity $v_{\perp d}/U_u$ is determined by three dimensionless parameters for this idealized problem: (i) the ratio of the downstream to the upstream magnetic field magnitude B_d/B_u; (ii) the ratio of the upstream perpendicular velocity to the upstream bulk-flow velocity $v_{\perp u}/U_u$; and (iii) the gyrophase θ of the ion† when it first reaches $x = 0$. In Fig. 1(a), the specific ion trajectory plotted returns upstream (red segment) due to the increased magnetic field downstream of the discontinuity. If the ion does *not* return upstream to $x > 0$, then one can compute the downstream perpendicular velocity $v_{\perp d}/U_u$ as the difference between the velocity upon crossing the discontinuity and the downstream

† Note that, since the inflow velocity is in the $-x$ direction for the model configurations considered in this study, we define gyrophase θ as the angle measured *clockwise* from the $-x$ direction. Therefore, $\theta = 0$ corresponds to a perpendicular velocity that increases the magnitude of the inflow velocity, and $\theta = 180^\circ$ decreases the magnitude of the inflow velocity.

$\mathbf{E}\times\mathbf{B}$ velocity, yielding

$$\frac{v_{\perp d,th}}{U_u}=\left\{\left[\frac{v_{\perp u}}{U_u}\cos\theta+\left(1-\frac{B_u}{B_d}\right)\right]^2+\left[\frac{v_{\perp u}}{U_u}\sin\theta\right]^2\right\}^{1/2} \tag{4.1}$$

Note that, although the perpendicular energy relative to the local (upstream or downstream) bulk-flow velocity generally increases, this increase comes at the expense of the kinetic energy of the incoming bulk flow, and the total kinetic energy of each ion is conserved in this process. This statement can be proven for a ring of ions with perpendicular velocity $v_{\perp u}$ about upstream velocity U_u by squaring (4.1), substituting $B_d/B_u=U_u/U_d$, integrating the gyrophase θ over 2π, and multiplying by $m_i/2$, to obtain the expression,

$$\frac{1}{2}m_i v_{\perp d,th}^2=\frac{1}{2}m_i v_{\perp u}^2+\frac{1}{2}m_i(U_u-U_d)^2. \tag{4.2}$$

The conservation of energy is obvious when evaluated in the downstream frame ($U_d=0$), where (4.2) proves that the downstream perpendicular energy of the ring of ions is simply the sum of the upstream perpendicular energy plus the "bulk" kinetic energy of the ring distribution moving at U_u.

If the ion does return upstream, it can gain energy by the process of shock-drift acceleration, since the transverse (to the shock normal) component of the Larmor velocity is in the same direction as the motional electric field that supports the inflow at the $\mathbf{E}\times\mathbf{B}$ velocity. Therefore, the rate of work done on the ion is $qv_yE_y>0$, and the ion gains energy above the prediction given by (4.1).

The energy gain by shock drift acceleration in this idealized model† can be plotted as a function of the $v_{\perp u}/U_u$ and θ on the (v_x,v_y) plane, leaving the single remaining parameter B_d/B_u. In Fig. 7, we plot the gain of perpendicular energy $(v_{\perp d}/v_{\perp d,th})^2$ as a function of (v_x,v_y) for $B_d/B_u=4,3,2$ in panels (a,b,c). In this figure, the black contours separate regions with different numbers of crossings of the $x=0$ plane, where every ion must cross the $x=0$ plane an odd number of times, given by the large numbers on the plot. The increase of the perpendicular energy due to shock drift acceleration is given by the colorbar. All ions that cross the $x=0$ plane only once conserve their energy, leading to the increase of the perpendicular energy (relative to the downstream frame) predicted by (4.1) (green color).

Note that only ions within a specific range of gyrophase angles and with sufficient perpendicular energy will be reflected upstream and gain energy due to the shock-drift acceleration mechanism. For the $B_d/B_u=4$ case in Fig. 7(a), we see that ions with $v_{\perp u}/U_u=0.3$ (blue circle) will reflect over the gyrophase angle range $17^\circ<\theta<102^\circ$ (blue). The minimum perpendicular velocity, relative to the inflow velocity, required for any ions to reflect increases with a decreasing value of the jump in the magnetic field, B_d/B_u. We find that for ions to reflect, the perpendicular velocity must have a value (a) $v_{\perp u}/U_u\geqslant 0.23$ for $B_d/B_u=4$, (b) $v_{\perp u}/U_u\geqslant 0.46$ for $B_d/B_u=3$, and (c) $v_{\perp u}/U_u\geqslant 0.79$ for $B_d/B_u=2$. Note that, if we take the upstream sound speed to be approximately equal to the ion thermal velocity, $c_s\simeq v_{tu}$, then the ratio of the perpendicular velocity of the reflected ions to the upstream ion thermal velocity can be expressed approximately by $v_{\perp u}\simeq v_{tu}\sim M_s(v_{\perp u}/U_u)$. Therefore, given the threshold values for reflection $v_{\perp u}/U_u$ determined above, this means that only ions in the tail of the velocity distribution (and

† Note that the ions must gain energy at the expense of the field energy, but this simple single-particle-motion analysis is not self-consistent and therefore does not account for the loss of field energy needed to conserve total energy.

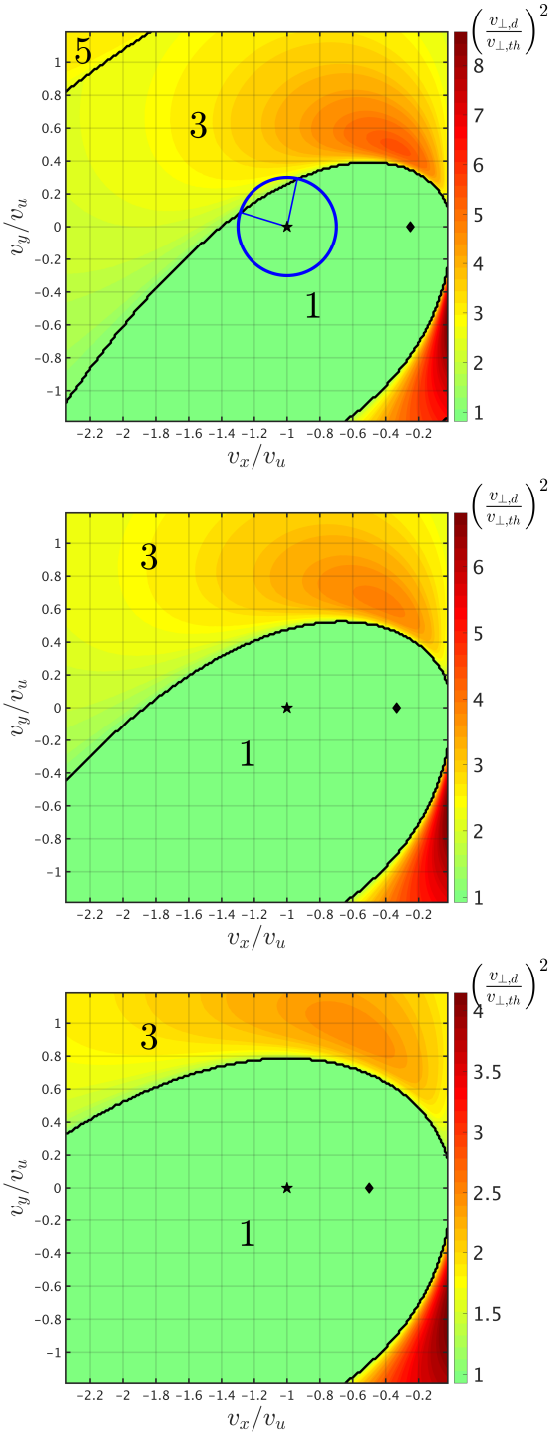

FIGURE 7. Ion energization as a function of $v_{\perp u}/U_u$ and θ on the (v_x, v_y) plane for $B_d/B_u =$ (a) 4, (b) 3, and (c) 2. The upstream bulk velocity is given by the star, the downstream bulk velocity is given by the diamond. .

within the range of initial gyrophase angles θ that yield reflection) will reflect and gain energy through shock-drift acceleration.

Although this simple model of ion energization at a magnetic discontinuity neglects a number of important characteristics of real collisionless shocks, such as a finite-width ramp or a cross shock potential, it nontheless provides an important foundation upon which to interpret simulations and observations of collisionless shocks. In particular, it shows that ion energy is conserved unless the ion crosses the discontinuity more than once, although the energy is transformed from upstream bulk-flow kinetic energy to perpendicular energy about the downstream bulk flow.

5. Discussion and Conclusion

This paper presents the first attempt to apply the field-particle correlation technique to understand particle energization in collisionless shocks. We tackle the specific case of an exactly perpendicular collisionless shock, investigating the particle enegization in two limits of the ratio of the particle Larmor radius ρ_s to the shock ramp width L: (i) ion enegization in the limit $\rho_i/L \gtrsim 1$, and (ii) electron energization in the limit $\rho_e/L \ll 1$.

Ion energization is explored in an idealized model of a perpendicular collisionless shock as a magnetic discontinuity with a amplitude jump $B_d/B_u = 4$, corresponding to the limit $\rho_i/L \gg 1$. A single-particle-motion analysis following the trajectory of particles through both configuration and velocity space shows that ions that are reflected at the shock transition are energized in the shock foot region by the motional electric field, a process known as *shock drift acceleration* (Anagnostopoulos *et al.* 1998; Ball & Melrose 2001; Lever *et al.* 2001; Park *et al.* 2013). A Vlasov-mapping technique (Scudder *et al.* 1986; Kletzing 1994; Hull *et al.* 1998; Hull & Scudder 2000; Hull *et al.* 2001; Mitchell & Schwartz 2013, 2014) is used to predict the evolution of the entire ion velocity distribution, showing a clear signature of reflected ions in the foot region consistent with previous theoretical and observational studies (Paschmann *et al.* 1982; Sckopke *et al.* 1983; Gedalin *et al.* 2018). Application of the field-particle correlation technique to this case yielded the first key result of this study, the velocity-space signature of the shock drift acceleration of ions in the shock foot, shown in Fig. 3(b). Notably, the field-particle correlation analysis makes clear that the ion energization is dominated here by the reflected population, while the incoming ion beam experiences negligible energization.

Electron energization is investigated using an idealized model of a perpendicular collisionless shock as a linear ramp of magnetic field magnitude of finite width $L = 2d_i$, corresponding to the limit $\rho_e/L \ll 1$. A single-particle-motion analysis shows that the electrons are energized by the motional electric field in the shock ramp due to the ∇B drift of the electrons caused by the gradient of the perpendicular magnetic field in the normal direction, conserving the magnetic moment of the electrons $\mu = m_e v_\perp^2/2B_z$ as the plasma drifts at the $\mathbf{E} \times \mathbf{B}$ velocity up the magnetic field ramp. The second key result of this study is the application of the field-particle correlation technique to determine the velocity-space signature of adiabatic electron heating, shown in Fig. 5(d), (f), and (h). The asymmetry of the electron energization is highlighted by cuts through these velocity-space signatures along v_y through the center of the distribution, shown in Fig. 6.

The theoretical work presented here provides an essential foundation for the interpretation of the velocity-space signatures of particle energization in collisionless shocks using the field-particle correlation technique applied to kinetic numerical simulations or spacecraft observations. We have identified clear velocity space signatures of the shock drift acceleration of ions in the shock foot and of adiabatic electron heating within the shock

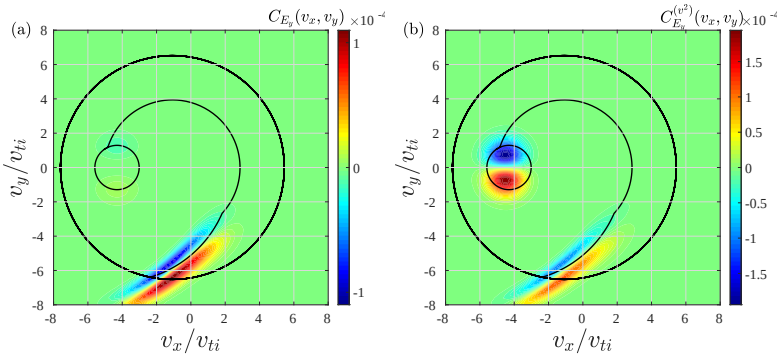

FIGURE 8. Component vs. full correlation example. .

ramp. The intuition gained by this theoretical investigation will be used to interpret the velocity-space signatures of particle energization from a field-particle correlation analysis of a 1D-2V Vlasov simulation of a perpendicular shock using the `Gkeyll` simulation code, to be present in the companion Paper II (Juno *et al.* 2020).

This first application of the field-particle correlation technique to examine particle energization in collisionless shocks has focused strictly on the idealized case of an exactly perpendicular shock with $\theta_{Bn} = 90°$ in the supercritical regime with fast magnetosonic Mach number $M_f = 3$. Future theoretical studies will tackle the particle energization in perpendicular shocks over a range of Mach numbers with the possibility of multiple reflections of particles at the shock front (Caprioli *et al.* 2015), as well as the higher dimensional problem of quasi-perpendicular shocks with $45° \leqslant \theta_{Bn} < 90°$. Furthermore, missing from the non-self-consistent single-particle-motion and Vlasov-mapping analyses presented here is the feedback of the free energy in the non-thermal particle velocity distributions onto the fields via kinetic instabilities, which may generate fluctuations in the fields that modify the resulting particle energization in the shock transition. To explore these important additional physical processes, self-consistent kinetic simulations are needed to determine how they alter the mechanisms of particle energization at the shock. Application of the field-particle correlation technique will enable us to understand how such instabilities alter the velocity-space signatures of the ion and electron energization in both kinetic numerical simulation and spacecraft observations.

GGH, JJ, JMT, DC, and AS were supported by NASA grant 80NSSC20K1273. GGH was also supported by NASA grants 80NSSC18K1366 80NSSC18K1217, 80NSSC18K1371, and 80NSSC18K0643. JMT was supported by DOE grant DE-SC0020049. LBW was partially supported by Wind MO & DA grants and a Heliophysics Innovation Fund (HIF) grant. DC was partially supported by NASA (grant NNX17AG30G, 80NSSC18K1218, and 80NSSC18K1726), NSF (grants AST-1714658, AST-1909778, PHY-1748958). AS was supported by NSF grants PHY-1804048 and AST-1814708. GGH, JJ, DC, and AS were partially supported by the "Multiscale Phenomena in Plasma Astrophysics" program at the Kavli Institute for Theoretical Physics (NSF grant PHY-1748958). LBW and DC were partially supported by the International Space Science Institute's (ISSI) International Teams program.

Appendix A. Form of Field-Particle Correlation

In the correlations $C_{E_x}(v_x, v_y)$ and $C_{E_y}(v_x, v_y)$, defined by (1.3) and (1.4), we have chosen to replace the v^2 in the second term on the right-hand side of (1.1) by v_x^2 in

(1.3) and v_y^2 in (1.4). This simplification is justified because, although this change indeed alters the rate of change of phase-space energy density as a function of velocity space (v_x, v_y), the difference in these two forms vanishes upon integration of the field-particle correlation over velocity space. In other words, the change does not alter the net rate of particle energization at a given spatial position $\mathbf{r}_0$. That this replacement does not alter the net rate of energization is easily seen by examining the x contribution to the dot product in the second term of (1.1) when integrated over (v_x, v_y) velocity space,

$$\begin{aligned}
&\int_{-\infty}^{-\infty} dv_x \int_{-\infty}^{-\infty} dv_y \left(-q_s \frac{(v_x^2 + v_y^2)}{2} E_x \frac{\partial f_s}{\partial v_x} \right) \\
&= -\frac{q_s}{2} E_x \int_{-\infty}^{-\infty} dv_y \left[\int_{-\infty}^{-\infty} dv_x v_x^2 \frac{\partial f_s}{\partial v_x} + v_y^2 \cancelto{0}{\int_{-\infty}^{-\infty} dv_x \frac{\partial f_s}{\partial v_x}} \right] \\
&= \int_{-\infty}^{-\infty} dv_x \int_{-\infty}^{-\infty} dv_y \left(-q_s \frac{v_x^2}{2} E_x \frac{\partial f_s}{\partial v_x} \right) \qquad \text{(A 1)}
\end{aligned}$$

where the v_x integral of the factor with v_y^2 is a perfect differential, and thus contributes nothing since $\lim_{v_x \to \pm\infty} f(v_x, v_y) = 0$.

The primary motivation for this substitution is to highlight the regions in velocity space that contribute to the net energy transfer between the particles and fields. Let us define an alternative form of the y-component of the field-particle correlation by $C_{E_y}^{(v^2)}$ that uses the full v^2 factor, given by

$$C_{E_y}^{(v^2)}(\mathbf{v}, t, \tau) = C\left(-q_s \frac{v^2}{2} \frac{\partial f_s(\mathbf{r}_0, \mathbf{v}, t)}{\partial v_y}, E_y(\mathbf{r}_0, t) \right). \qquad \text{(A 2)}$$

In Fig. 8, we plot the two forms of the field-particle correlation (a) C_{E_y} and (b) $C_{E_y}^{(v^2)}$ for the same case shown in Fig. 3(a) and (b). Using the alternative form in Fig. 8(b) $C_{E_y}^{(v^2)}$ given by (A 2), we see that there is a large feature in the velocity-space signature of the ion energization associated with the incoming ion flow, but that significant feature leads to zero net ion energization. In fact, apparent energy transfer associated with E_y in this form is actually canceled exactly by the magnetic field term $(\mathbf{v} \times \mathbf{B})_x \partial f / \partial v_x$ in the Lorentz force, as discussed in Appendix E.

Using the preferred form in Fig. 8(a) C_{E_y}, this net zero energy transfer associated with the incoming ion beam does not appear. Only the energy transfer associated with the reflected ions appears when using the form in (1.4). Therefore, although using only the v_y^2 contribution does not capture the full energy flow in (v_x, v_y) velocity space, it does capture the energy transfer associated with the net rate of energization, and so this form is preferable for the study of particle energization in collisionless shocks.

Appendix B. Complementary Eulerian and Lagrangian Approaches

The field-particle correlation technique yields an Eulerian description of the particle energization in the six-dimensional (3D-3V) phase space of the kinetic plasma description. In other words, it determines the rate of change of phase-space energy density $w_s(\mathbf{r}_0, \mathbf{v}_0)$ at a fixed point in $(\mathbf{r}_0, \mathbf{v}_0)$ in 3D-3V phase space. Because modern spacecraft instrumentation can return the full 3V velocity distribution function at the spatial position of the spacecraft $\mathbf{r}_0$, the ability of the field-particle correlation technique to determine the rate of change of $w_s(\mathbf{r}_0, \mathbf{v}_0)$ over the full 3V velocity space at that point $\mathbf{r}_0$ makes

Alfvén speed, v_A	$v_A^2 = B_0^2/4\pi n_0 m_i$
Sound speed, c_s	$c_s^2 = \gamma(T_i + T_e)/m_i$
Fast Magnetosonic velocity, v_f	$v_f^2 = v_A^2 + c_s^2$
Species Thermal Velocity, v_{ts}	$v_{ts}^2 = 2T_s/m_s$
Fluid Total Plasma Beta, β	$\beta = c_s^2/v_A^2$
Individual Species Plasma Beta, β_s	$\beta_s = 8\pi n_s T_s/B^2$
Alfvén Mach number, M_A	$M_A = U_x/v_A$
Sonic Mach Number, M_s	$M_s = U_x/c_s$
Fast Magnetosonic Mach Number, M_f	$M_f = U_x/v_f$

TABLE 1. Definitions of characteristic velocities, plasma beta values, and Mach numbers. Note the Boltzmann's constant has been absorbed into the temperature, giving temperature in units of energy.

it well-suited for application to observational measurements. In contrast, historically, the numerical investigation of collisionless shocks has traditionally used a particle-in-cell (PIC) description of the particle velocity distribution (using either fully kinetic PIC or hybrid PIC approaches). The analysis of particle-based simulation codes often tracks the change of energy of a macro-particle as it follows its trajectory through six-dimensional (3D-3V) phase space. Therefore, particle-based codes naturally represent a Lagrangian description of the kinetic plasma dynamics.

Numerical simulation codes based on either Eulerian continuum (grid-based) or on Lagrangian particle-based velocity-space descriptions have complementary advantages and disadvantages in the study of collisionless shocks: (i) continuum (grid-based) velocity-space descriptions provide the full particle velocity distribution functions at each point in configuration space without the $\sqrt{N}$ noise inherent to the random (or Monte Carlo) sampling of velocity space in particle-based codes; but (ii) particle-based codes can track the acceleration of particles to very high energies that are not represented within the maximum energies of velocity-space grids in continuum codes. These complementary capabilities motivate the effort to make a clear connection between the more traditional Lagrangian view of particle energization at collisionless shocks and the less common Eulerian point-of-view that arises naturally using the field-particle correlation technique. A key goal of this paper is to make clear that connection using a single-particle-motion analysis to connect the Lagrangian view of the dynamics of a single particle along its trajectory through the shock transition to an Eulerian view of the evolution of the entire particle velocity distribution at a single position in the shock structure. For example, for the case of 1D-2V shock simulations, the physics is often studied examining (x, v_x) phase-space plots, but here we aim to develop an intuitive picture of the full 2V distribution function (v_x, v_y) at a single point as a function of distance from the shock along the normal direction. Because the full distribution function (v_x, v_y) at a single point is an observationally accessible quantity using modern spacecraft instrumentation, developing this intuition is a valuable goal for maximizing the scientific return from spacecraft measurements of collisionless shocks.

Appendix C. Definitions of the Plasma and Shock Parameters

Table 1 provides definitions of relevant characteristic velocities, plasma beta values, and Mach numbers. We consider a quasineutral proton-electron plasma equilibrium, $n_{0i} = n_{0e}$, a realistic mass ratio $m_i/m_e = 1836$, and we absorb the Boltzmann constant into T_s, giving temperature in units of energy. Note that $\beta = \gamma/2(\beta_i + \beta_e) = \gamma/2[v_{ti}^2/v_A^2 +$

$v_{te}^2/v_A^2(m_e/m_i)]$, where $\gamma = 5/3$ is the adiabatic index. In terms of the plasma beta values, we have $c_S/v_A = \sqrt{\gamma/2(\beta_i + \beta_e)}$ and $v_f/v_A = \sqrt{1+\beta} = \sqrt{1+\gamma/2(\beta_i+\beta_e)}$.

Appendix D. Vlasov Mapping Technique to Determine Full Particle Velocity Distributions

We can explore the evolution of the particle velocity distributions in our idealized perpendicular shock models by a technique that we denote *Vlasov mapping* (Scudder *et al.* 1986; Kletzing 1994; Hull *et al.* 1998; Hull & Scudder 2000; Hull *et al.* 2001; Mitchell & Schwartz 2013, 2014). At the physical point $\mathbf{x}_{\rm obs}$ at which we want to "observe" the ion velocity distribution, we repeat the single-particle-motion analysis for every point $(v_{x,\rm init}, v_{y,\rm init})$ in the velocity space, integrating backwards in time until we reach a point $\mathbf{x}_{\rm up}$ upstream in the unperturbed, inflowing plasma. This backwards integration yields a final position in velocity space $(v_{x,\rm fin}, v_{y,\rm fin})$ by following along the ion trajectory through phase space. Since the ion velocity distribution upstream is known, we know the phase-space density at this final point in velocity space $(v_{x,\rm fin}, v_{y,\rm fin})$. For a collisionless plasma, Liouville's theorem dictates that the phase-space density is invariant along the particle trajectories through 3D-3V phase space, so we may set the phase-space energy density at $(v_{x,\rm init}, v_{y,\rm init})$ at the point of observation equal to the phase-space density upstream at $(v_{x,\rm fin}, v_{y,\rm fin})$, giving

$$f_i(\mathbf{x}_{\rm obs}, v_{x,\rm init}, v_{y,\rm init}) = f_i(\mathbf{x}_{\rm up}, v_{x,\rm fin}, v_{y,\rm fin}). \tag{D 1}$$

This Vlasov mapping technique is, of course, not self-consistent with respect to how the evolving particle velocity distributions may become unstable and generate electromagnetic field fluctuations through kinetic instabilities. It is essentially an extension of the single-particle-motion analysis, computing the evolution of the full velocity distribution due to known electromagnetic fields. Furthermore, it is possible in general that regions of phase-space downstream do not connect to any position upstream, leading to voids in the downstream phase space, but for the perpendicular collisionless shock evaluated here, we have not encountered this potential difficulty.

Appendix E. Calculation of Field-Particle Correlation for the $\mathbf{E}\times\mathbf{B}$ Drift

Here we calculate the field-particle correlation for the rate of change of phase-space energy density in the region upstream of the shock. Consider the case, relevant to the particular transverse magentized shock problem addressed here, of a constant transverse magnetic field $\mathbf{B} = B_{z0}\hat{\mathbf{z}}$ and a constant electric field $\mathbf{E} = -E_{y0}\hat{\mathbf{y}}$ where $E_{y0} > 0$, giving an upstream $\mathbf{E}\times\mathbf{B}$ velocity of $\mathbf{u}_{E\times B} = -(E_{y0}/B_{z0})\hat{\mathbf{x}}$.

The 2V Maxwellian distribution in the upstream region is given by

$$f_s(v_x, v_y) = \frac{n_0}{\pi v_{ts}^2} e^{-[(v_x - u_{E\times B})^2 + v_y^2]/v_{ts}^2} \tag{E 1}$$

With no spatial variation in the upstream region, the rate of change of phase-space energy density $w_s(x, v_x, v_y, t) \equiv m_s v^2 f_s(x, v_x, v_y, t)/2$ is given by

$$\frac{\partial w_s(\mathbf{r}, \mathbf{v}, t)}{\partial t} = -q_s \frac{v^2}{2} \left(\mathbf{E} + \mathbf{v}\times\mathbf{B}\right) \cdot \frac{\partial f_s}{\partial \mathbf{v}}. \tag{E 2}$$

Substituting in the fields and the velocity-space derivatives

$$\frac{\partial f_s}{\partial v_x} = \frac{-2(v_x - u_{E\times B})}{v_{ts}^2} f_s \tag{E 3}$$

$$\frac{\partial f_s}{\partial v_y} = \frac{-2v_y}{v_{ts}^2} f_s, \tag{E 4}$$

we obtain the following result

$$\frac{\partial w_s(\mathbf{r},\mathbf{v},t)}{\partial t} = -q_s \frac{v^2}{2} \left(-v_y E_{y0} - \cancel{v_x v_y B_{z0}} + \cancel{v_y v_x B_{z0}} - v_y u_{E\times B} B_{z0}\right) \frac{2f_s}{v_{ts}^2} \tag{E 5}$$

where we see that the term from $(\mathbf{v}\times\mathbf{B})_y (\partial f_s/\partial v_y)$ cancels with the contribution from $(\mathbf{v}\times\mathbf{B})_x (\partial f_s/\partial v_x)$ that is not associated with the $\mathbf{E}\times\mathbf{B}$ flow. Now, if we substitute for the $\mathbf{E}\times\mathbf{B}$ velocity, where $u_{E\times B} = -(E_{y0}/B_{z0})$, we obtain

$$\frac{\partial w_s(\mathbf{r},\mathbf{v},t)}{\partial t} = -q_s \frac{v^2}{2} \left(\cancel{-v_y E_{y0}} - \cancel{v_y \left[-\frac{E_{y0}}{B_{z0}}\right] B_{z0}}\right) \frac{2f_s}{v_{ts}^2} = 0, \tag{E 6}$$

where the change of phase-space energy density due to the electric field in the first term is canceled by the change of phase-space energy density due to the magnetic field acting on the $\mathbf{E}\times\mathbf{B}$ flow.

Note that in the analysis presented in §3, we compute only the energy transfer in velocity space associated with E_y contribution to the Lorentz force term. Although the net rate of electron energization in Fig. 5(b) is zero, one may get the false impression that the rate of change of phase-space energy is non-zero in the positive and negative regions of the velocity-space signature. However, as the calculation above demonstrates, the work done by the $E_y \partial f/\partial v_y$ term in the Lorentz force, plotted in Fig. 5(b), is exactly canceled by the $u_{E\times B}$ contribution in the magnetic field term $(\mathbf{v}\times\mathbf{B})_x \partial f/\partial v_x$ term in the Lorentz force.

The lesson here is that, if one cares only about the net rate of particle energization, evaluation of the electric field contributions to the rate of change of phase-space energy density is sufficient to capture the salient details of the net particle energization. But, if one further wants to determine the total rate of change of phase-space energy density at each point in (v_x, v_y) velocity space, one needs to evaluate all of the terms in (1.1), including the magnetic field contributions to the Lorentz force and the heat flux contributions associated with the ballistic term. When evaluating the electric field correlations alone, one must always keep in mind that one is only diagnosing part of the rate of change of phase-space energy density, albeit it is the only part that leads to a net change of particle energy, which is typically the ultimate goal.

REFERENCES

Afshari, A. S., Howes, G. G., Kletzing, C. A., Hartley, D. P. & Boardsen, S. A. 2020 Electron landau damping of turbulence in the terrestrial magnetosheath plasma. *Geophys. Res. Lett.* Submitted.

Anagnostopoulos, G. C., Rigas, A. G., Sarris, E. T. & Krimigis, S. M. 1998 Characteristics of upstream energetic (E⩾50keV) ion events during intense geomagnetic activity. *J. Geophys. Res.* **103**, 9521–9534.

Ball, Lewis & Melrose, D. B. 2001 Shock Drift Acceleration of Electrons. *Pub. Astron. Soc. Australia* **18** (4), 361–373.

Blandford, R. & Eichler, D. 1987 Particle acceleration at astrophysical shocks: A theory of cosmic ray origin. *Phys. Rep.* **154**, 1–75.

Blandford, R. D. & Ostriker, J. P. 1978 Particle acceleration by astrophysical shocks. *Astrophys. J.* **221**, L29–L32.

Caprioli, D., Amato, E. & Blasi, P. 2010 Non-linear diffusive shock acceleration with free-escape boundary. *Astropart. Phys.* **33**, 307–311.

Caprioli, Damiano, Pop, Ana-Roxana & Spitkovsky, Anatoly 2015 Simulations and Theory of Ion Injection at Non-relativistic Collisionless Shocks. *Astrophys. J. Lett.* **798** (2), L28.

Caprioli, D. & Spitkovsky, A. 2014 Simulations of Ion Acceleration at Non-relativistic Shocks. I. Acceleration Efficiency. *Astrophys. J.* **783** (2), 91.

Chen, C. H. K., Klein, K. G. & Howes, G. G. 2019 Evidence for electron Landau damping in space plasma turbulence. *Nature Comm.* **10** (1), 740.

Chen, L. J., Wang, S., Wilson, L. B., Schwartz, S., Bessho, N., Moore, T., Gershman, D., Giles, B., Malaspina, D., Wilder, F. D., Ergun, R. E., Hesse, M., Lai, H., Russell, C., Strangeway, R., Torbert, R. B., F. -Vinas, A., Burch, J., Lee, S., Pollock, C., Dorelli, J., Paterson, W., Ahmadi, N., Goodrich, K., Lavraud, B., Le Contel, O., Khotyaintsev, Yu. V., Lindqvist, P. A., Boardsen, S., Wei, H., Le, A. & Avanov, L. 2018 Electron Bulk Acceleration and Thermalization at Earth's Quasiperpendicular Bow Shock. *Phys. Rev. Lett.* **120** (22), 225101.

Decker, R. B. 1988 The role of drifts in diffusive shock acceleration. *Astrophys. J.* **324**, 566–573.

Edmiston, J. P. & Kennel, C. F. 1984 A parametric survey of the first critical Mach number for a fast MHD shock. *J. Plasma Phys.* **32** (3), 429–441.

Ellison, D. C. 1983 Diffusive first-order Fermi acceleration at quasi-parallel interplanetary shocks - Injection of thermal ions. *Proc. 18th Intl. Cosmic Ray Conf.* **10**, 108–111.

Fermi, E. 1949 On the Origin of the Cosmic Radiation. *Phys. Rev.* **75**, 1169–1174.

Fermi, E. 1954 Galactic Magnetic Fields and the Origin of Cosmic Radiation. *Astrophys. J.* **119**, 1.

Gedalin, M. 1996*a* Ion reflection at the shock front revisited. *J. Geophys. Res.* **101** (A3), 4871–4878.

Gedalin, M. 1996*b* Transmitted ions and ion heating in nearly perpendicular low-Mach number shocks. *J. Geophys. Res.* **101** (A7), 15569–15578.

Gedalin, M. 1997 Ion heating in oblique low-Mach number shocks. *Geophys. Res. Lett.* **24** (20), 2511–2514.

Gedalin, M., Newbury, J. A. & Russell, C. T. 2000 Numerical analysis of collisionless particle motion in an observed supercritical shock front. *J. Geophys. Res.* **105** (A1), 105–114.

Gedalin, Michael, Zhou, Xiaoyan, Russell, Christopher T., Drozdov, Alexander & Liu, Terry Z. 2018 Ion Dynamics and the Shock Profile of a Low-Mach Number Shock. *J. Geophys. Res.* **123** (11), 8913–8923.

Goodrich, K. A., Ergun, R. E., Schwartz, S. J., Wilson III, L. B., Newman, D., Wilder, F. D., Holmes, J., Johlander, A., Burch, J. L., Torbert, R. B., Khotyaintsev, Yu., Lindqvist, P.-A., Russell, C. T., Gershman, D. J., Giles, B. L. & Andersson, L. 2018 MMS Observations of Electrostatic Waves in an Oblique Shock Crossing. *J. Geophys. Res.* **123** (11), 9430–9442.

Gosling, J. T., Thomsen, M. F., Bame, S. J. & Russell, C. T. 1989 Ion reflection and downstream thermalization at the quasi-parallel bow shock. *J. Geophys. Res.* **94**, 10027–10037.

Howes, G. G. 2017 A prospectus on kinetic heliophysics. *Phys. Plasmas* **24** (5), 055907.

Howes, G. G., Klein, K. G. & Li, T. C. 2017 Diagnosing collisionless energy transfer using field-particle correlations: Vlasov-Poisson plasmas. *J. Plasma Phys.* **83** (1), 705830102.

Howes, G. G., McCubbin, A. J. & Klein, K. G. 2018 Spatially localized particle energization by Landau damping in current sheets produced by strong Alfvén wave collisions. *J. Plasma Phys.* **84** (1), 905840105.

Hull, A. J. & Scudder, J. D. 2000 Model for the partition of temperature between electrons and ions across collisionless, fast mode shocks. *J. Geophys. Res.* **105** (A12), 27323–27342.

Hull, A. J., Scudder, J. D., Frank, L. A., Paterson, W. R. & Kivelson, M. G. 1998

Electron heating and phase space signatures at strong and weak quasi-perpendicular shocks. *J. Geophys. Res.* **103** (A2), 2041–2054.

Hull, A. J., Scudder, J. D., Larson, D. E. & Lin, R. 2001 Electron heating and phase space signatures at supercritical, fast mode shocks. *J. Geophys. Res.* **106** (A8), 15711–15734.

Jokipii, J. R. 1987 Rate of Energy Gain and Maximum Energy in Diffusive Shock Acceleration. *Astrophys. J.* **313**, 842.

Juno, J., Howes, G. G., TenBarge, J. M. & others 2020 A field-particle correlation analysis of a perpendicular magnetized collisionless shock: Ii. vlasov simulations. *J. Plasma Phys.* Submitted.

Kennel, C. F., Edmiston, J. P. & Hada, T. 1985 A quarter century of collisionless shock research. *Washington DC American Geophysical Union Geophysical Monograph Series* **34**, 1–36.

Klein, K. G. 2017 Characterizing fluid and kinetic instabilities using field-particle correlations on single-point time series. *Phys. Plasmas* **24** (5), 055901.

Klein, K. G. & Howes, G. G. 2016 Measuring Collisionless Damping in Heliospheric Plasmas using Field-Particle Correlations. *Astrophys. J. Lett.* **826**, L30.

Klein, K. G., Howes, G. G. & TenBarge, J. M. 2017 Diagnosing collisionless enegy transfer using field-particle correlations: gyrokinetic turbulence. *J. Plasma Phys.* **83** (4), 535830401.

Klein, K. G., Howes, G. G., TenBarge, J. M. & Valentini, F. 2020 Diagnosing collisionless energy transfer using field-particle correlations: Alfvén-ion cyclotron turbulence. *J. Plasma Phys.* Submitted.

Kletzing, C. A. 1994 Electron acceleration by kinetic Alfvén waves. *J. Geophys. Res.* **99**, 11095–11104.

Leroy, M. M. & Mangeney, A. 1984 A theory of energization of solar wind electrons by the earth's bow shock. *Ann. Geophys.* **2**, 449–456.

Lever, Edward L., Quest, Kevin B. & Shapiro, Vitali D. 2001 Shock surfing vs. shock drift acceleration. *Geophys. Res. Lett.* **28** (7), 1367–1370.

Li, Tak Chu, Howes, Gregory G., Klein, Kristopher G., Liu, Yi-Hsin & TenBarge, Jason M. 2019 Collisionless energy transfer in kinetic turbulence: field–particle correlations in fourier space. *Journal of Plasma Physics* **85** (4), 905850406.

Malkov, M. A. & Drury, L. O. 2001 Nonlinear theory of diffusive acceleration of particles by shock waves. *Rep. Prog. Phys.* **64**, 429–481.

Mitchell, J. J. & Schwartz, S. J. 2013 Nonlocal electron heating at the Earth's bow shock and the role of the magnetically tangent point. *J. Geophys. Res.* **118** (12), 7566–7575.

Mitchell, J. J. & Schwartz, S. J. 2014 Isothermal magnetosheath electrons due to nonlocal electron cross talk. *J. Geophys. Res.* **119** (2), 1080–1093.

Park, J., Caprioli, D. & Spitkovsky, A. 2015 Simultaneous Acceleration of Protons and Electrons at Nonrelativistic Quasiparallel Collisionless Shocks. *Phys. Rev. Lett.* **114** (8), 085003.

Park, J., Ren, C., Workman, J. C. & Blackman, E. G. 2013 Particle-in-cell Simulations of Particle Energization via Shock Drift Acceleration from Low Mach Number Quasi-perpendicular Shocks in Solar Flares. *Astrophys. J.* **765**, 147.

Paschmann, G., Sckopke, N., Bame, S. J. & Gosling, J. T. 1982 Observations of gyrating ions in the foot of the nearly perpendicular bow shock. *Geophys. Res. Lett.* **9** (8), 881–884.

Sagdeev, R. Z. 1966 Cooperative Phenomena and Shock Waves in Collisionless Plasmas. *Rev. Plasma Phys.* **4**, 23.

Sagdeev, R. Z. & Shapiro, V. D. 1973 Influence of Transverse Magnetic Field on Landau Damping. *Sov. Phys.–JETPL* **17**, 279–282.

Savoini, P., Lembége, B. & Stienlet, J. 2010 Origin of backstreaming electrons within the quasi-perpendicular foreshock region: Two-dimensional self-consistent PIC simulation. *J. Geophys. Res.* **115**, 9104.

Sckopke, N., Paschmann, G., Bame, S. J., Gosling, J. T. & Russell, C. T. 1983 Evolution of ion distributions across the nearly perpendicular bow shock - Specularly and non-specularly reflected-gyrating ions. *J. Geophys. Res.* **88**, 6121–6136.

Sckopke, N., Paschmann, G., Brinca, A. L., Carlson, C. W. & Luehr, H. 1990 Ion thermalization in quasi-perpendicular shocks involving reflected ions. *J. Geophys. Res.* **95** (A5), 6337–6352.

Scudder, J. D., Mangeney, A., Lacombe, C., Harvey, C. C., Wu, C. S. & Anderson, R. R. 1986 The resolved layer of a collisionless, high β, supercritical, quasi-perpendicular shock wave, 3. Vlasov electrodynamics. *J. Geophys. Res.* **91** (A10), 11075–11098.

Shapiro, V. D. & Üçer, D. 2003 Shock surfing acceleration. *Planet. Space Sci.* **51**, 665–680.

Shuster, J. R., Gershman, D. J., Chen, L. J., Wang, S., Bessho, N., Dorelli, J. C., da Silva, D. E., Giles, B. L., Paterson, W. R., Denton, R. E., Schwartz, S. J., Norgren, C., Wilder, F. D., Cassak, P. A., Swisdak, M., Uritsky, V., Schiff, C., Rager, A. C., Smith, S., Avanov, L. A. & Viñas, A. F. 2019 MMS Measurements of the Vlasov Equation: Probing the Electron Pressure Divergence Within Thin Current Sheets. *Geophys. Res. Lett.* **46** (14), 7862–7872.

Thomsen, M. F., Gosling, J. T., Bame, S. J. & Mellott, M. M. 1985 Ion and electron heating at collisionless shocks near the critical Mach number. *J. Geophys. Res.* **90** (A1), 137–148.

Treumann, R. A. 2009 Fundamentals of collisionless shocks for astrophysical application, 1. Non-relativistic shocks. *Astron. Astrophys. Rev.* **17** (4), 409–535.

Wilson III, L. B. 2016 Low frequency waves at and upstream of collisionless shocks. In *Low-frequency Waves in Space Plasmas* (ed. A. Keiling, D.-H. Lee & V. Nakariakov), *Geophys. Monogr. Ser.*, vol. 216, pp. 269–291. Washington, D.C.: American Geophysical Union.

Wilson III, L. B., Cattell, C. A., Kellogg, P. J., Goetz, K., Kersten, K., Kasper, J. C., Szabo, A. & Wilber, M. 2010 Large-amplitude electrostatic waves observed at a supercritical interplanetary shock. *J. Geophys. Res.* **115**, 12104.

Wilson III, L. B., Koval, A., Szabo, A., Breneman, A., Cattell, C. A., Goetz, K., Kellogg, P. J., Kersten, K., Kasper, J. C., Maruca, B. A. & Pulupa, M. 2012 Observations of electromagnetic whistler precursors at supercritical interplanetary shocks. *Geophys. Res. Lett.* **39**, 8109.

Wilson III, L. B., Sibeck, D. G., Breneman, A. W., Le Contel, O., Cully, C., Turner, D. L., Angelopoulos, V. & Malaspina, D. M. 2014*a* Quantified Energy Dissipation Rates in the Terrestrial Bow Shock: 1. Analysis Techniques and Methodology. *J. Geophys. Res.* **119** (8), 6455–6474.

Wilson III, L. B., Sibeck, D. G., Breneman, A. W., Le Contel, O., Cully, C., Turner, D. L., Angelopoulos, V. & Malaspina, D. M. 2014*b* Quantified Energy Dissipation Rates in the Terrestrial Bow Shock: 2. Waves and Dissipation. *J. Geophys. Res.* **119** (8), 6475–6495.

Wu, C. S. 1984 A fast Fermi process - Energetic electrons accelerated by a nearly perpendicular bow shock. *J. Geophys. Res.* **89**, 8857–8862.